AGU PUBLICATIONS

JGR

Journal of Geophysical Research: Solid Earth

RESEARCH ARTICLE

10.1002/2014JB011727

Key Points:
- We investigate the position of mantle plumes post-supercontinent formation
- We analyze the role of subduction and mantle viscosity using numerical models
- Subcontinental plume locations show dependence on continental margin subduction

Correspondence to:
P. J. Heron,
philip.heron@utoronto.ca

Citation:
Heron, P. J., J. P. Lowman, and C. Stein (2015), Influences on the positioning of mantle plumes following supercontinent formation, *J. Geophys. Res. Solid Earth*, *120*, 3628–3648, doi:10.1002/2014JB011727.

Received 27 OCT 2014
Accepted 24 MAR 2015
Accepted article online 28 MAR 2015
Published online 13 MAY 2015

Influences on the positioning of mantle plumes following supercontinent formation

Philip J. Heron[1,2], Julian P. Lowman[1,3], and Claudia Stein[4]

[1]Department of Physics, University of Toronto, Toronto, Ontario, Canada, [2]Now at Department of Earth Sciences, University of Toronto, Toronto, Ontario, Canada, [3]Also at Department of Physical and Environmental Sciences, University of Toronto Scarborough, Toronto, Ontario, Canada, [4]Institut für Geophysik, Westfälische Wilhelms-Universität Münster, Germany

Abstract Several mantle convection studies analyzing the effects of supercontinent formation and dispersal show that the genesis of subcontinental plumes results from the formation of subduction zones at the edges of the supercontinent rather than from the effect of continental thermal insulation or thermochemical piles. However, the influence of subduction zone location on the position of subcontinental plumes has received little attention. This study analyzes 2-D and 3-D numerical models of supercontinent formation (in an isochemical mantle) to assess the role of subduction and mantle viscosity contrast in the generation of subcontinental mantle plumes. We find that once a critical supercontinent width is reached, plumes do not form under the center of a supercontinent. In studies featuring a low viscosity lower mantle, the surface positions of the initial plumes (arriving within 90 Myr of supercontinent assembly) become locked beneath the continent at a distance 2000–3000 km from the continental margin. However, the broad downwellings in simulations that feature a high-viscosity lower mantle trigger plumes at a greater distance from the continental margin subduction. For all mantle viscosity profiles, subcontinental plumes show dependence on the location of supercontinent margin subduction. As theories differ on the role of core-mantle boundary chemical piles in plume formation, it is significant that our isochemical models show that the formation of subduction zones at the margins of a supercontinent has a profound effect on subcontinental mantle dynamics. Our results may help to explain what determined the eruption sites of past (and future) large igneous provinces.

1. Introduction

Expansive areas of igneous material on the Earth's surface (e.g., large igneous provinces (LIPs) [*Burke and Torsvik*, 2004]) are thought to be manifestations of past thermal plume head arrivals. The plumes originated deep in the mantle and erupted over short geological timescales. The deep mantle origin of the large igneous provinces can be inferred from the generation of dyke swarms, surface uplift, and the geochemical signature of the erupted material [see *Courtillot et al.*, 1999; *Ernst et al.*, 2005]. Analyzing the rock record over Earth's history shows little LIP activity during the amalgamation stage of the supercontinent cycle [e.g., *Yale and Carpenter*, 1998; *Ernst et al.*, 2005; *Ernst and Bleeker*, 2010]. However, following a period of time after the supercontinent forms, the number of large igneous provinces increases on a global scale [e.g., *Yale and Carpenter*, 1998; *Ernst et al.*, 2005; *Ernst and Bleeker*, 2010]. Figure 1 (discussed further below) shows the paleopositions of 24 large igneous provinces with deposition ages dating back to 300 Ma (i.e., from the formation of Pangea to the present day) as projected downward onto the core-mantle boundary [*Torsvik et al.*, 2006, 2008]. A key observation of Figure 1 is that plumes do not form at the geographical center of Pangea near the suture zone, but rather toward the margins of the supercontinent.

The paleoposition of large igneous provinces has previously been attributed to plume generation zones (PGZs) at the edges of seismically observed large low shear velocity provinces (LLSVPs) situated beneath the present-day locations of Africa and the Pacific [*Torsvik et al.*, 2006; *Burke et al.*, 2008; *Torsvik et al.*, 2008, 2010; *Steinberger and Torsvik*, 2012]. This hypothesis requires the compositionally dense anomalies associated with LLSVPs to be relatively stationary over 500 Myr periods. However, recent thermochemical geodynamic models [e.g., *Zhang et al.*, 2010; *Tan et al.*, 2011; *Li and McNamara*, 2013] have shown difficulty in generating stable dense compositional piles on the timescales required by the static LLSVP hypothesis. Therefore, a secondary role for compositionally dense piles in the generation of subcontinental plumes has been suggested [*Davies et al.*, 2012].

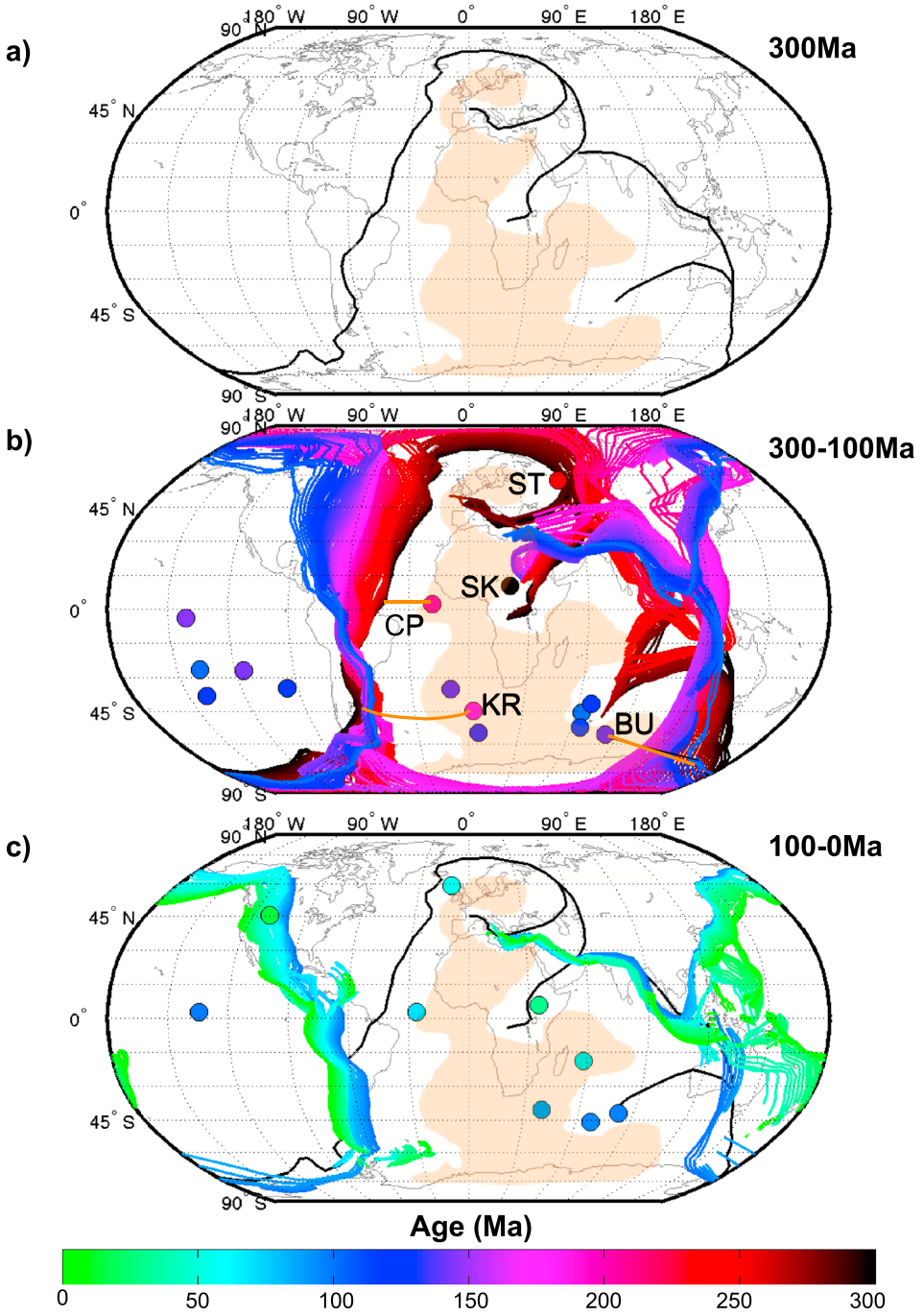

Figure 1. Subduction zone and large igneous province position. The positions of the subduction zones between 300 Ma and present [*Steinberger and Torsvik*, 2012] are plotted alongside the positions of 24 large igneous provinces (LIPs) between 300 and 0 Ma. The LIP positions have been corrected to their original paleoposition at the time of their deposition. The color of the subduction zone corresponds to the age at which subduction occurred and LIP color corresponds to the age at which formation occurred, respectively. The outline of the present-day (0 Ma) position of the continents, the paleosubduction at 300 Ma, and the "center" of the supercontinent Pangea (orange-shaded region) are shown as a reference on each panel. (a) Paleosubduction at 300 Ma highlights the area within which all continental material was positioned, the "center" of Pangea, and has been isolated from subduction since the Carboniferous (the shaded region represents 50% of the surface area of the site bounded by Pangea subduction). (b) Paleosubduction and LIP position between 300 Ma and 100 Ma. The Skagerrak (SK), Siberian Traps (ST), Central Atlantic Magmatic Province (CP), Karoo Ridge (KR), and Bunbury Basalts (BU) LIPs (and the nearest 300Ma subduction location) are highlighted. (c) Paleosubduction and LIP position between 100 Ma and 0 Ma. The subduction zone and LIP positions were determined by *Steinberger and Torsvik* [2012] and *Torsvik et al.* [2006, 2008], respectively.

An alternative hypothesis is that downwellings that reach the core-mantle boundary sweep aside compositionally dense piles [e.g., *Tackley*, 1998; *Kellogg et al.*, 1999; *Jellinek and Manga*, 2002; *McNamara and Zhong*, 2005] and that the current shape of LLSVPs is due to the Earth's subduction history (c.f., Figure 1) pushing chemically dense material into regions where they coalesce beneath upwelling volumes of the Earth's mantle [*McNamara and Zhong*, 2005; *Bull et al.*, 2009; *Zhang et al.*, 2010; *Tan et al.*, 2011; *Davies et al.*, 2012; *Li and McNamara*, 2013]. The theory that subduction can mould LLSVPs to control the location of upwellings is in opposition to the hypothesis that LLSVPs are stationary and that LIPs develop above the margins of LLSVPs. Given the presence of compositional anomalies, it is difficult to determine the primary influence on the position of plumes post-supercontinent formation: Are stationary LLSVPs forcing plumes to develop at PGZs, or does subducted material create PGZs while moulding LLSVPs that generate plumes?

Previous studies featuring an isochemical mantle showed that subduction dominates the development of plumes [e.g., *Schubert et al.*, 2004; *McNamara and Zhong*, 2005; *Zhong et al.*, 2007; *Santosh et al.*, 2009; *Zhang et al.*, 2010; *Heron and Lowman*, 2010; *Yoshida and Santosh*, 2011]. However, in many models plumes are generated far from the location of subduction and close to the center of a supercontinent, which is not in-keeping with the observations over the last 300 Myr (Figure 1).

Here, we reconsider the influence of subduction and mantle rheology on plume position in large-scale models of mantle dynamics post-supercontinent formation. The evolution of mantle dynamics is examined after supercontinent accretion, considering a range of continental coverage. Two-dimensional and three-dimensional Cartesian geometry mantle convection simulations are presented, featuring thermally and mechanically distinct oceanic and continental plates and geotherm- and intrinsically depth-dependent viscosity structure. Through changing the size of the supercontinent (and therefore the location of continental margin subduction), system length-scales affecting the generation of mantle plumes are analyzed considering purely thermal convection. In calculations featuring vigorous mantle convection, the upper and lower mantle viscosity contrast is also changed to determine its influence on plume formation. Finally, we investigate the influence of continental thermal insulation and global subduction zone migration on the thermal evolution of the subcontinental mantle.

2. Method

2.1. Governing Equations

Mantle convection is modeled using the hybrid finite-difference spectral method code MC3D [*Gable et al.*, 1991] to solve the dimensionless equations of mass, momentum, and energy conservation for an infinite Prandtl number Boussinesq fluid in a Cartesian geometry:

$$\vec{\nabla} \cdot \vec{u} = 0, \tag{1}$$

$$\vec{\nabla} \cdot \left[\eta \left(\vec{\nabla}\vec{u} + (\vec{\nabla}\vec{u})^T\right)\right] - \vec{\nabla}P = -Ra_0 T\hat{z} \tag{2}$$

and

$$\frac{\partial T}{\partial t} = \nabla^2 T - \vec{u} \cdot \vec{\nabla} T, \tag{3}$$

respectively. The nondimensional fields above (and how they are nondimensionalized, with nondimensional parameters now given by a prime) are $\vec{u}'(u = (\kappa_0/d)u')$, the velocity (where d is the dimensional depth of the mantle and κ_0 the dimensional surface thermal diffusivity); $\eta'(\eta = \eta_0\eta')$, the dynamic viscosity (which is both geotherm and inherently depth dependent) where η_0 is the dimensional surface dynamic viscosity; $P'(P = (\eta_0\kappa_0/d^2)P')$, the nonhydrostatic pressure; and $T'(T - T_0 = T'\Delta T)$, the temperature where T_0 is the dimensional surface temperature. ΔT is the superadiabatic temperature difference between the bottom and top boundaries. The height above the base of the mantle is z, and $t'(t = (d^2/\kappa_0)t')$ is time. Ra_0 is the reference Bénard-Rayleigh number [*Chandrasekhar*, 1961] and is given by

$$Ra_0 = \frac{\alpha\rho_0 g\Delta T d^3}{\kappa_0\eta_0}, \tag{4}$$

where g is the gravitational acceleration (which is antiparallel to $\hat{z}$); and α is the thermal expansivity. The system is completed by a linearized equation of state:

$$\rho = \rho_o(1 - \alpha(T - T_o)), \tag{5}$$

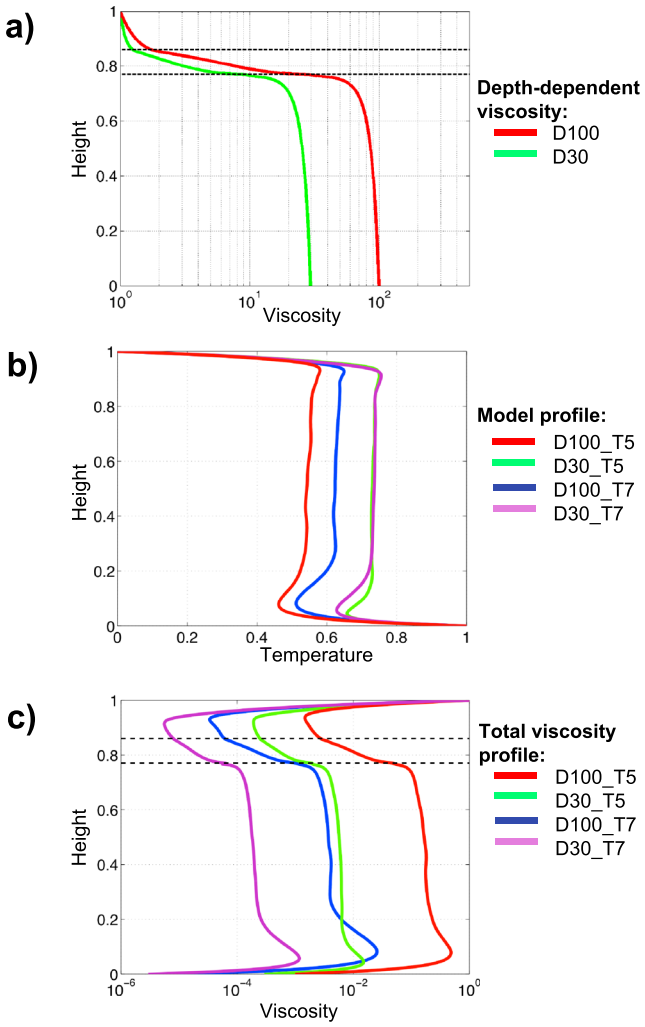

Figure 2. (a) Depth-dependent viscosity profiles (η_D) for cases D100 (red) and D30 (green), (b) initial condition nondimensional geotherms, and (c) viscosity (η') for 2-D study (Model D100_T5, red; D30_T5, green; D100_T7, blue; D30_T7, purple). Dashed lines in Figures 2a and 2c show the depths corresponding to 440 km and 660 km (defining the mantle transition zone). Model parameters are given in Table 1.

where ρ_o is the density obtained when $T = T_o$, the surface temperature (in this study, $T' = 0$ at the surface and $T' = 1$ at the core-mantle boundary).

2.2. Viscosity Structure and Surface Heat Flux

The nondimensional mantle viscosity, η', is calculated through the product of the nondimensional geotherm- and depth-dependent viscosities ($\eta' = \eta_{\bar{T}} \times \eta_D$). Models have a time-dependent viscosity resulting from the use of the horizontally averaged nondimensional mantle temperature (geotherm), $\bar{T}(z)$, in the calculation of $\eta_{\bar{T}}(z)$:

$$\eta_{\bar{T}} = \Delta\eta_T^{-\bar{T}}, \tag{6}$$

where $\Delta\eta_T$ is the nondimensional viscosity contrast owing to temperature. The range of nondimensional viscosity associated with the thermal viscosity contrast ($\Delta\eta_T$) is from 1 at the surface to ($1/\Delta\eta_T$) at the base of the mantle. As a result, an increase in $\Delta\eta_T$ will decrease the average viscosity of the model. The four viscosity models presented here also feature changes in the inherent depth-dependent viscosity contrast between the surface and the core-mantle boundary ($\eta_D(z)$ varies from 100 (model names prefixed D100*) to 30 (prefixed D30*), Figure 2a), in addition to changes in the thermal viscosity contrast, $\Delta\eta_T$, (from 10^5 (model names ending *T5) to 10^7 (*T7)). Within this range, the response of the calculations to changes in model viscosity structure is

Table 1. Input Parameters and Initial Condition Properties for the 2-D Models[a]

Model	η_D	$\Delta\eta_T$	$\bar{q}_{surf}$	Ra_0	Ra_{avg}	T_L	v_{rms}	v_p	M	<T>
D100_T5	100	10^5	23	2.5×10^5	2.0×10^7	0.35	2000	4600	2.3	0.54
D30_T5	30	10^5	23	7.0×10^4	5.5×10^7	0.35	3300	2600	0.8	0.71
D100_T7	100	10^7	23	8.0×10^3	2.9×10^7	0.40	1800	3500	1.9	0.60
D30_T7	30	10^7	23	1.5×10^3	3.7×10^7	0.45	2400	2800	1.2	0.69

[a] η_D refers to the contrast in the intrinsic depth-dependent viscosity profile, and $\Delta\eta_T$ is the thermal viscosity contrast. $\bar{q}_{surf}$, v_{rms}, <T>, T_L, and M refer to the average surface heat flux, system root-mean-square velocity, volume-averaged mantle temperature, lithospheric cut-off temperature, and mobility ratio, respectively. The mobility ratio, M, is the ratio of surface plate velocity (v_P) to v_{rms}. If M is > 0.5, a mobile tectonic regime exists. Ra_0 is the Rayleigh number obtained with the surface viscosity, where T' is 0 ($\eta' = 1$). Ra_{avg} is the average Rayleigh number calculated from the product of the inverse of the average nondimensional horizontal viscosity and the reference Ra_0. The $\bar{q}_{surf}$ values are matched by changing the reference Rayleigh number, Ra_0, and plate velocities vary by less than a factor of two for models with different viscosity parameters. The grid resolutions of the models are 2501 × 201 (D100_T5) or 2501 × 401 (D30_T5 and *T7).

analyzed. There is no lateral variation in viscosity when using this depth- and geotherm-dependent viscosity condition. Table 1 shows the viscosity parameters for the models featured in this study.

Heron and Lowman [2014] showed that the effect of Rayleigh number in determining the influence of supercontinents on mantle convection is important. In low Ra supercontinent formation calculations, different dynamic behavior is generated compared to (more Earth-like) high Ra simulations. Large mantle upwelling and downwelling features in low Ra ($\sim 10^5$) calculations produced amplified horizontal upper mantle flow and a relatively high core-mantle boundary increase in heat flux (when compared to high Ra models) [*Heron and Lowman*, 2014]. Consequently, we model high convective vigor throughout this study. For example, the mantle parameters of Model D100_T5 ($Ra_0 = 2.5 \times 10^5$ (Table 1)) generate a plate thickness of 0.018*d* (52 km), a nondimensional heat flux of 23 (estimated to be 20–30 for the Earth), and an average Rayleigh number, Ra_{avg}, of 2.0×10^7 (where Ra_{avg} is defined as

$$Ra_{avg} = Ra_0 \overline{\left(\frac{1}{\eta'(z)} \right)}, \tag{7}$$

Ra_0 is the Rayleigh number obtained with the surface viscosity (where T' is 0 ($\eta' = 1$)), and $\overline{\eta'(z)^{-1}}$ is the average of the inverse of the viscosity). Utilizing Earth-like values for the parameters in the Rayleigh number [e.g., *Hofmeister*, 1999; *Schubert et al.*, 2001] gives an effective Ra for the Earth of $\sim 10^7$. The convective vigor in the Cartesian models presented here can be considered Earth-like if Ra_{avg} is 10^7 or higher. Figure 2 shows the component of depth-dependent viscosity (Figure 2a), temperature as a function of depth (geotherm) (Figure 2b), and the total mantle viscosity (Figure 2c) for the four different profiles. Figure 2c shows that the viscosity profiles vary by orders of magnitude. In order to ensure that the vigor of the convection in all models is high and similar, mantle parameters (as outlined in section 2.3) are adjusted so that the initial surface heat flux values in each case are matched to that of Model D100_T5 (see Table 1).

Recently, for plane-layer convection models with an Earth-like Rayleigh number, *O'Farrell and Lowman* [2010] showed that either no internal heating or a degree of mantle cooling is necessary to attain the spherical shell-type geotherms that occur with terrestrial concentrations of internal heating. Accordingly, we do not specify any internal heating in the models presented here.

2.3. Plate Velocities, Plate Thickness, and Plate Boundary Mobility

All calculations feature plate-like surface velocity behavior obtained by modeling dynamically determined, time-dependent, horizontal velocity boundary conditions. Plate velocities are continuously updated using a force-balance method [*Gable et al.*, 1991; *King et al.*, 1992; *Brandenburg and van Keken*, 2007] which requires that the total of the integrated shear tractions at the base of each plate is zero. Global plate velocity that neither adds to nor subtracts from system energy is obtained by balancing the forces from buoyancy and viscous resistance, where the latter acts on the plates due to their motion. This method of calculating plate velocities is consistent with a strong rigid plate uniformly distributing applied stresses and has been shown to yield plate velocities and heat flux values in agreement with modeling methods that utilize rheologically defined plates [e.g., *King et al.*, 1992; *Koglin et al.*, 2005; *Stein et al.*, 2013, 2014]. In all models, the continent (also

referred to as "supercontinent") is stationary (i.e., the continental plate has no plate velocity and its boundaries do not migrate) as in the case of the inferred history of Pangea's evolution [*Scotese*, 2001]. Only the oceanic plates have velocities that are determined by the force-balance calculation (which includes the influence of the stationary supercontinent).

In the majority of the models presented, plate boundaries do not evolve. However, in one 3-D case we couple MC3D with a finite element mesh generation code (LaGriT) to calculate the motion of plate boundaries determined by a set of conditions that simulate plate tectonic evolution. Specifically, the oceanic triple junctions move with a velocity equal to the area weighted mean of the adjacent plates [e.g., *Gait et al.*, 2008; *Stein and Lowman*, 2010]; continental plate boundaries do not evolve.

We model a lithosphere-asthenosphere transition as a mechanical boundary above which the mantle is sufficiently cool to behave in a more stiff manner and below which the mantle material deforms more readily. The plate thickness (δ) is determined by the depth at which the geotherm (laterally averaged temperature) exceeds a given lithospheric cut-off temperature (T_L), with the average plate viscosity being ~2 orders of magnitude greater than the viscosity of the mantle immediately below. At the time-dependent depth, δ, the force-balance calculation is applied. As a result, both the oceanic and continental plates have a spatially uniform but time-dependent thickness. Continental plates are given distinct thermal and mechanical properties that generate mantle insulation.

Figures 2b and 2c shows the horizontally averaged temperature (geotherm) and the nondimensional viscosity profile for the initial condition of the calculations in the 2-D study. The thin surface boundary layer shown by the geotherms is indicative of a high vigor of convection (Figure 2b). The two depth-dependent viscosity profiles in this study ($\eta_D = 30$ and 100, Figure 2a) act to mitigate the effect of the thermal viscosity contrast [*Zhong et al.*, 2000] (Figure 2c). Implementing a thermally dependent lithospheric thickness allows our plate modeling method to display a transition from mobile to stagnant-lid convection when internal heating is increased [*Heron*, 2014], as is observed in models that obtain plate-like surface motion through the incorporation of temperature- and stress-dependent rheologies [e.g., *Stein et al.*, 2004, 2013]. The choice of the nondimensional lithospheric cut-off temperature (T_L) is important due to its effect on plate mobility (and therefore mantle temperatures). A nondimensional T_L value of either 0.35 (models D100_T5 and D30_T5), 0.40 (D100_T7), or 0.45 (D30_T7) is specified to ensure that the plates move within a mobility (M) range (defined by the ratio of surface to interior root-mean-square velocity (v_{rms}) values) that is in-keeping with mobile-lid behaviour (e.g., greater than 0.5 [*Tackley*, 2000; *Stein et al.*, 2013]).

2.4. Continental Insulation

Continental insulation is prescribed by limiting the ability of the continental plate to conduct heat. Here, the thermal diffusivity of the continental region, κ_c, is reduced in comparison to the oceanic lithosphere, while the oceanic plates have the thermal conductivity of the mantle. Consequently, the continental plate is a relatively greater insulator. It should be noted that distinct oceanic and continental plate thicknesses [e.g., *Lenardic et al.*, 2005, 2011; *Rolf et al.*, 2012] are not modeled. However, by prescribing an insulating diffusivity in the high viscosity continental material, it is possible to mimic the thermal blanketing effect of thick continental lithosphere. A continental diffusivity value of 0.25 of the oceanic value is chosen for the continental insulation parameter (i) for this study. The effective thickness of the continental lithosphere for this continental diffusivity value can be interpreted by considering the thermal diffusion timescale

$$\tau_p = \frac{L^2}{\kappa_c}, \tag{8}$$

which characterizes the time taken (τ_p) for a temperature change to diffuse a distance L (the continental lithosphere thickness). By setting $\kappa_c = 0.25\kappa$, the continent effectively insulates as if its thickness were double that of an oceanic plate. For models with no continental insulation prescribed, the continental plate region has the same thermal diffusivity as the oceans ($\kappa_c = \kappa$).

2.5. Temperature-Dependent Viscosity

The viscosity implemented here has no lateral variation and is therefore not fully temperature dependent. However, our methodology captures fluctuations in thermal boundary layer thickness and accompanying changes in the depths over which associated viscosity contrasts occur. Furthermore, through applying geotherm- and depth-dependent viscosity, we obtain a time-dependent lithospheric thickness capable of modelling a spectrum of different plate tectonic regimes (e.g., mobile and stagnant-lid convection). The

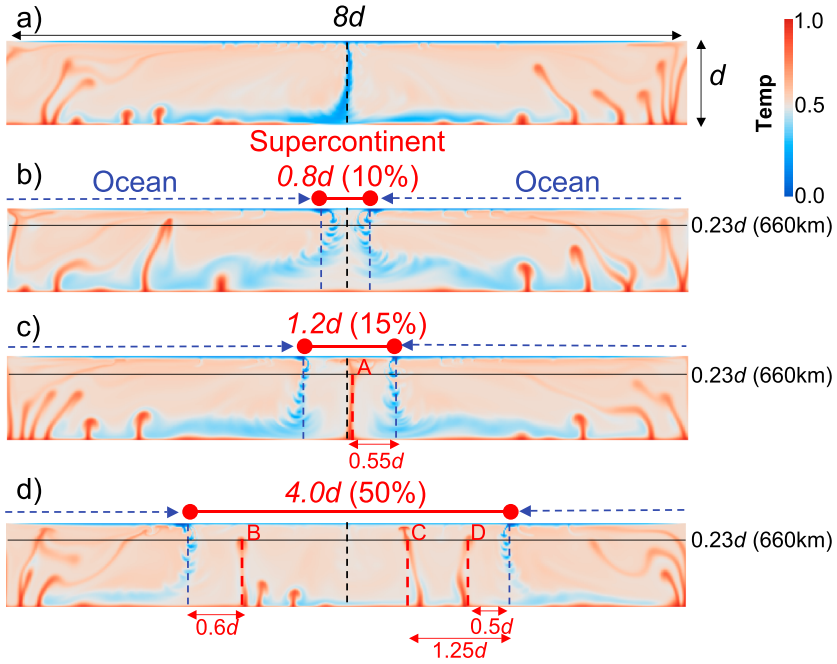

Figure 3. 2-D temperature snapshots of Model D100_T5 showing the initial condition and location of subcontinental plumes for different supercontinent models. All 2-D models initially feature a convergent plate boundary where continental material converges (analogous to the formation of Pangea [e.g., *Santosh et al.*, 2009]), as well as periodic sidewalls and an aspect ratio (Γ) 8 solution domain. Plumes are measured at 660 km (shown in nondimensional terms as 0.23*d*). (a) Supercontinent formation initial condition (t = 0 Myr). (b) Snapshot from model with a supercontinent covering 10% (0.8*d*, 2320 km) of the surface (t = 375 Myr). (c) Snapshot from model with collided continents covering 15% (1.2*d*, 3480 km) of the surface (t = 150 Myr). (d) Snapshot from model with a supercontinent covering 50% (4.0*d*, 11,600 km) of the surface (t = 64 Myr). Model parameters are given in Table 1.

transitions we observe between regimes are similar to results from models featuring pressure, temperature, and stress-dependent rheologies [e.g., *Moresi and Solomatov*, 1995; *Stein et al.*, 2004; *O'Neill and Lenardic*, 2007; *van Heck and Tackley*, 2008; *Foley and Becker*, 2009; *Korenaga*, 2010; *Stein et al.*, 2013, 2014]. In addition, *Stein and Hansen* [2014] showed layered temperature-dependent viscosity convection to be a suitable approximation to the full temperature dependence. When comparing mantle convection models featuring a geotherm-dependent viscosity (as used here) and fully temperature dependent viscosity, *Stein and Hansen* [2014] found only minor differences in flow characteristics (including Nusselt number, convection flow regime, lid thickness, stress, and dynamic topography).

3. 2-D Results

The effect on plume dynamics of mantle viscosity and supercontinent size is investigated here through studying the positions of new plumes post-supercontinent formation. Timescales are converted by scaling 60 Myr to one mantle transit time, τ (calculated by using the mantle v_{rms} and the time required to travel the depth of the mantle).

3.1. Initial Condition and Supercontinent Modeling

The initial conditions for all 2-D models are obtained through modeling mantle convection with a dynamic two-plate system. Snapshots of the evolution of these models are shown so that the convergent plate boundary appears on the vertical midplanes of the depicted temperature fields (see Figure 3a). Once the two-plate system reaches a statistically steady state (i.e., no long term heating or cooling trends are evident in the solution), the plate geometry is modified. A continental plate (with a prescribed velocity of zero) is centered over the initial downwelling between oceanic plates on each side (e.g., Figures 3b–3d). The emplacement of the continental plate simulates the collision of two equal width smaller continental plates at the site of the initial mantle downwelling. Continental insulation prior to collision is not considered. The supercontinent remains stationary (similar to the inferred history of Pangea's evolution [*Scotese*, 2001]) for the duration of the calculations described.

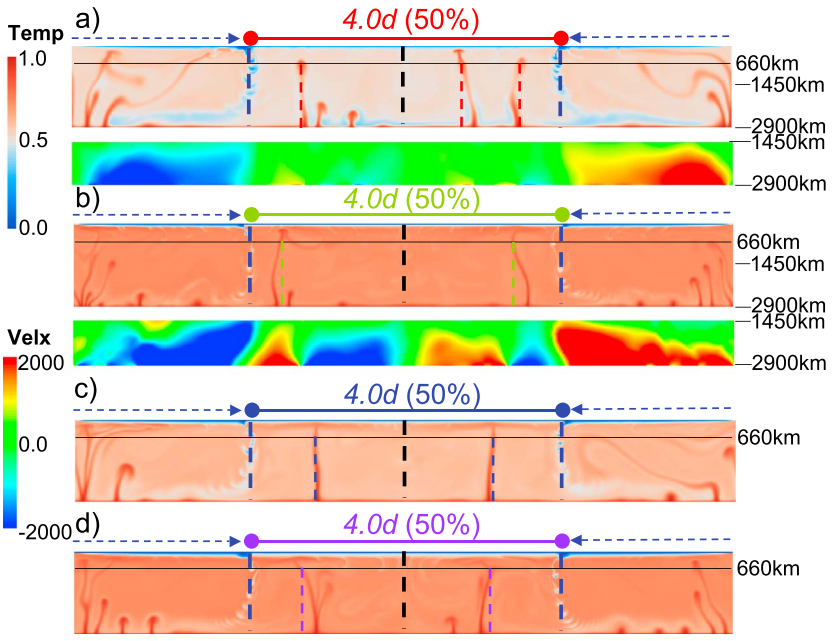

Figure 4. 2-D temperature snapshots for all models with supercontinent covering 50% (4.0*d*) of the surface. (a) Model D100_T5; (b) Model D30_T5; (c) Model D100_T7; (d) Model D30_T7. Model parameters are given in Table 1. Snapshots correspond to the arrival of the first set of plumes subsupercontinent (~60 My after supercontinent formation). Nondimensional horizontal velocity snapshots for the bottom half of Figures 4a and 4b are shown below the temperature snapshots.

3.2. Plume Position as a Function of Subduction Location

Figure 3 shows examples of different plume positions as a function of subduction zone (convergent plate boundary) location for a range of D100_T5 cases. For a supercontinent width of 0.8*d* (10% of the surface, corresponding to a dimensional width of 2320 km) (Figure 3b), plumes fail to form below the continent (indicating that plumes only develop subcontinent after a critical supercontinent width has been exceeded [e.g., *Gurnis*, 1988; *Zhong and Gurnis*, 1993; *Lowman and Jarvis*, 1995; *Trubitsyn and Rykov*, 1995; *Yoshida et al.*, 1999; *Honda et al.*, 2000; *Heron and Lowman*, 2011]). Increasing the size of the supercontinent to 1.2*d* (3480km) allows thermal instabilities to develop in the lower thermal boundary layer under the supercontinent and generate a subcontinental plume. The middle of a plume conduit reaches the upper mantle (e.g., depths less than 0.23*d* (660 km)) at a distance of 0.55*d* (1595 km) from the nearest subduction zone (e.g., the edge of the supercontinent) and therefore close to the plane of the continental suture (shown by the black dashed line in Figure 3c). Only the locations of the initial arrival plumes are recorded (where "initial arrivals" are defined as plumes that arrive in the upper mantle within 90 Myr post-supercontinent formation). Plume movement is not tracked. Primary plumes are defined as the first plumes to arrive post-supercontinent formation (and can include more than one plume if they arrive at approximately the same time). Secondary plumes are those that arrive after the primary plume and within the time frame of "initial" plumes (i.e., in the first 90 Myr after supercontinent formation). The choice of having a cut-off time period to analyze subcontinental plumes is motivated by our model not featuring a dispersing continents. To study the position of plumes after the first and second sets of upwellings was not considered relevant (even as a first-order approximation to mantle dynamics) as the timeframe exceeds the longevity of an assembled supercontinent. As a result, only plumes satisfying the "initial plume" definition are analyzed. For models with a single-plume system (e.g., small continental area), the initial timeframe is increased to 150 Myr to allow time for thermal anomalies to develop (e.g., Figure 3c).

Figure 3 shows that for the model parameters in D100_T5, the size of the continent (and repositioning of subduction zones) has an effect on the number (and location) of the subcontinental plumes in our model. However, changing the viscosity structure (e.g., η_D and $\Delta\eta_T$) of the models also has an effect on plume formation. Figure 4 shows the difference in plume locations and average mantle temperature across the range of 2-D calculations featuring supercontinents covering 4.0*d* of the surface (after the supercontinent forms through continental collisions at an initial downwelling (e.g., Figure 3a)). In this study, decreasing η_D from 100 to 30 for

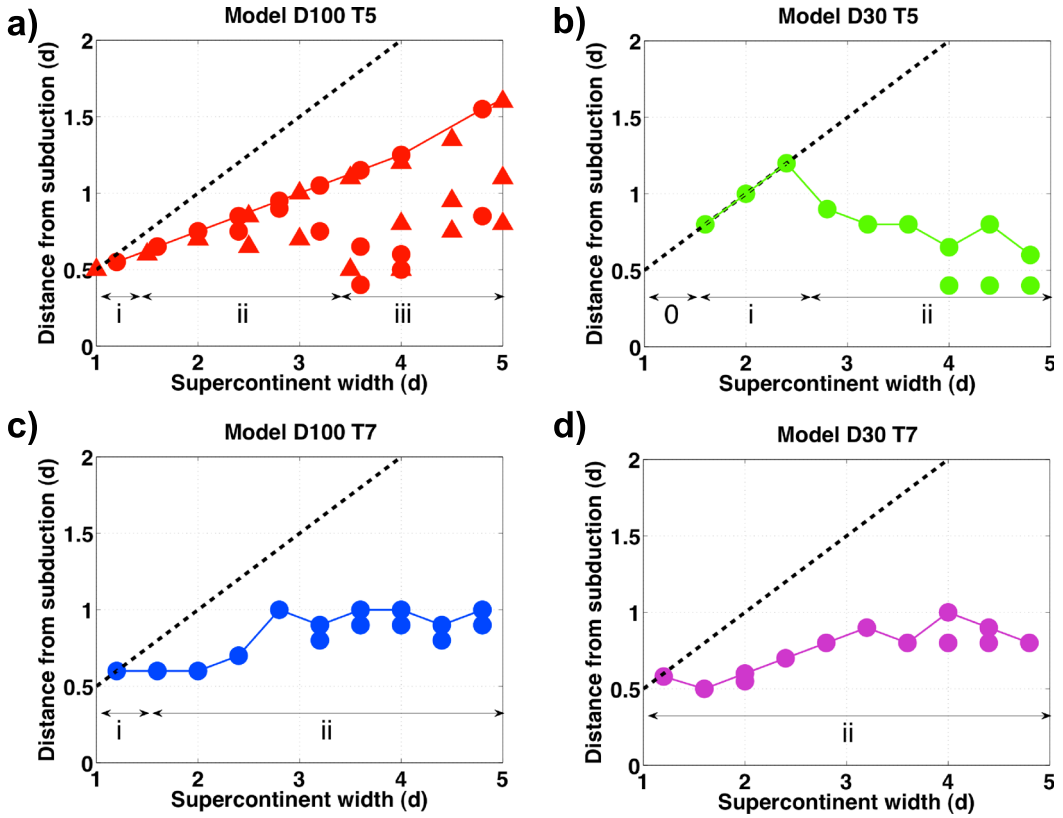

Figure 5. Plume position (circles) relative to continental margin location as a function of supercontinent coverage (with measurements given in units of mantle depth, *d*). Dashed line indicates the location of the continental suture. The location of the subcontinental plumes that arrive first (i.e., primary plumes) are connected by lines. (a) Model D100_T5; (b) Model D30_T5; (c) Model D100_T7; (d) Model D30_T7. Lower-case roman numerals show the number of initial plumes generated subcontinent (i.e., plumes generated within the first 90Myr (or 150 Myr for mono-plume systems) following supercontinent formation). Model parameters are given in Table 1. Triangles in Figure 5a correspond to D100_T5 calculations in a Γ=10 box.

models featuring $\Delta\eta_T = 10^5$ reduces the number of plumes that initially develop subcontinent (from three to two when comparing Figure 4a (D100_T5) and Figure 4b (D30_T5)). Furthermore, Model D30_T5 features subcontinent upwellings that form closer to the subduction zones on the margins of the supercontinent, in comparison to the locations observed in Model D100_T5. Models D100_T7 (Figure 4c) and D30_T7 (Figure 4d) show subcontinental plumes at similar locations. Therefore, increasing $\Delta\eta_T$ to 10^7 (Figures 4c and 4d) appears to supersede the effect of changing the depth-dependent viscosity.

The relation between plume position and supercontinent margin location, as a function of supercontinent coverage, for Models D100_T5, D30_T5, D100_T7, and D30_T7, is summarized in Figure 5. Increasing continental coverage for D100_T5 models (Figure 5a) generates primary subcontinental plumes located further away from the edges of the supercontinent. As shown in Figure 3, the number of initial plumes generated subcontinent increases with growing continental coverage. A possible explanation as to why more plumes form under the larger continents that feature the viscosity profile D100_T5, rather than any of the other viscosity profiles (Figure 5), is that the relatively high lower mantle viscosity (i.e., compared to the surface reference viscosity) retards velocities at the base of the mantle. Snapshots of the horizontal velocity field for models D100_T5 and D30_T5 are shown in Figures 4a and 4b, respectively. Subcontinental horizontal velocity close to the core-mantle boundary is very low in the D100_T5 case and very high for the D30_T5 model. The stagnation of the lower mantle leads to thermal instabilities on the core-mantle boundary that form closer to the continental suture location (e.g., D100_T5 Figures 4a and 5a) than in calculations featuring a diminished lower mantle viscosity (e.g., D30_T5 Figures 4b and 5b). The interaction between the remnant thermal field produced from the continental suture subduction and the flow driven by the new subduction combines to generate thermal gradients (that produce plumes). If the viscosity is relatively low at the base of the mantle,

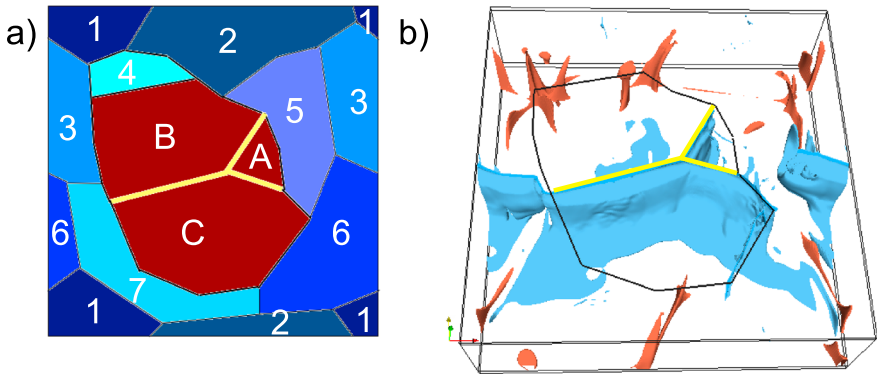

Figure 6. 3-D plate geometry and thermal initial condition at time of supercontinent formation. Continental collision is modeled along a Y-shaped configuration of convergent plate boundaries. (a) Plate geometry pre-supercontinent formation (where plates A, B, and C combine to form 30% of the model surface (note coverages of 15%, 20%, and 25% are also considered; see Figure 7a) surrounded by seven oceanic plates). (b) Temperature snapshot of the initial condition (for Model D100_T5 3D) showing the Y-shaped downwelling pattern. The nondimensional temperature isosurfaces of 0.25, 0.3, 0.35 (subducted oceanic lithosphere), and 0.8 (plumes) are shown, with the top 6% and bottom 3% of the model removed to allow for better viewing of the interior. The stencil of the supercontinent plate geometry covering 30% of the surface is shown on the top of the box (these rendering parameters are used in subsequent figures).

then the remnant thermal field from the initial subduction drives thermal anomalies away from the center of the supercontinent (e.g., D30_T5 Figure 4b). As a result, plumes form close to where new downwellings impact the thermal boundary layer at the base of the mantle. However, if the viscosity in the lower mantle is high relative to the reference viscosity, then the growth of thermal instabilities is slowed (e.g., velocity beneath the supercontinent in Figure 4a) and they form closer to the site of initial subduction (below the continental suture). Plumes are produced in the thermal boundary layer wherever there exists a strong thermal gradient. Hence, if the flow velocity in the lower mantle is relatively low, plumes can form both in close proximity to the continental suture subduction location and the margins of the supercontinent (Figure 4a). However, if the lower mantle viscosities are low relative to the reference viscosity, and therefore the lower mantle flow velocities comparatively high, plumes only form close to the continental margins (Figures 4b and 5).

Figure 5a shows results from both aspect ratio (Γ) 8 (circles) and $\Gamma = 10$ (triangles) D100_T5 models. As the aspect ratio was increased, a different initial condition was produced (however, supercontinent formation remains modeled as in the cases shown in Figure 3). The positions of the primary plumes are found to be similar for calculations with both aspect ratios (Figure 5a). This finding indicates the evolution of a subcontinent environment that is independent of the initial condition and solution domain aspect ratio.

In Model D30_T5 for supercontinent coverage $\geq 1.6d$ (4640 km) and $\leq 2.4d$ (6960 km) (Figure 5b), a subcontinental plume forms directly below the continental suture (if continental coverage is $< 1.6d$, no subcontinental plume forms). However, for continental coverage $> 2.4d$, the primary subcontinental plumes form between $0.6d$ and $0.9d$ (1740–2610 km) from the supercontinent margins. The results of Figures 5a and 5b indicate that reducing the lower mantle viscosity could lock continental plume position to new circum-supercontinent subduction zones rather than promoting plume formation below the continental suture. Through increasing the thermal viscosity contrast ($\Delta\eta_T$), the major differences between the two depth-dependent viscosity models essentially vanishes (Figures 5c and 5d). For continental coverage $\geq 2.8d$, both Model D100_T7 (Figure 5c) and D30_T7 (Figure 5d) feature subcontinental plume locations that fluctuate between $0.8d$ (2320 km) and $1.0d$ (2900 km) from the subduction at the edge of the supercontinent. This indicates that the repositioning of subduction zones to the supercontinent margins plays a strong role in the evolution of subcontinental dynamics and highlights the independence of subcontinental plume positioning from continental suture location.

4. 3-D Results

The effect on plume position of decreasing the depth-dependent viscosity contrast is now considered in 3-D calculations that use the parameters of D100_T5 (section 4.2) and D30_T5 (section 4.3). The effects of continental insulation (section 4.4) and evolving oceanic boundaries (section 4.5) on the generation of subcontinental thermal instabilities are also analyzed. Unless specified otherwise, a nondimensional

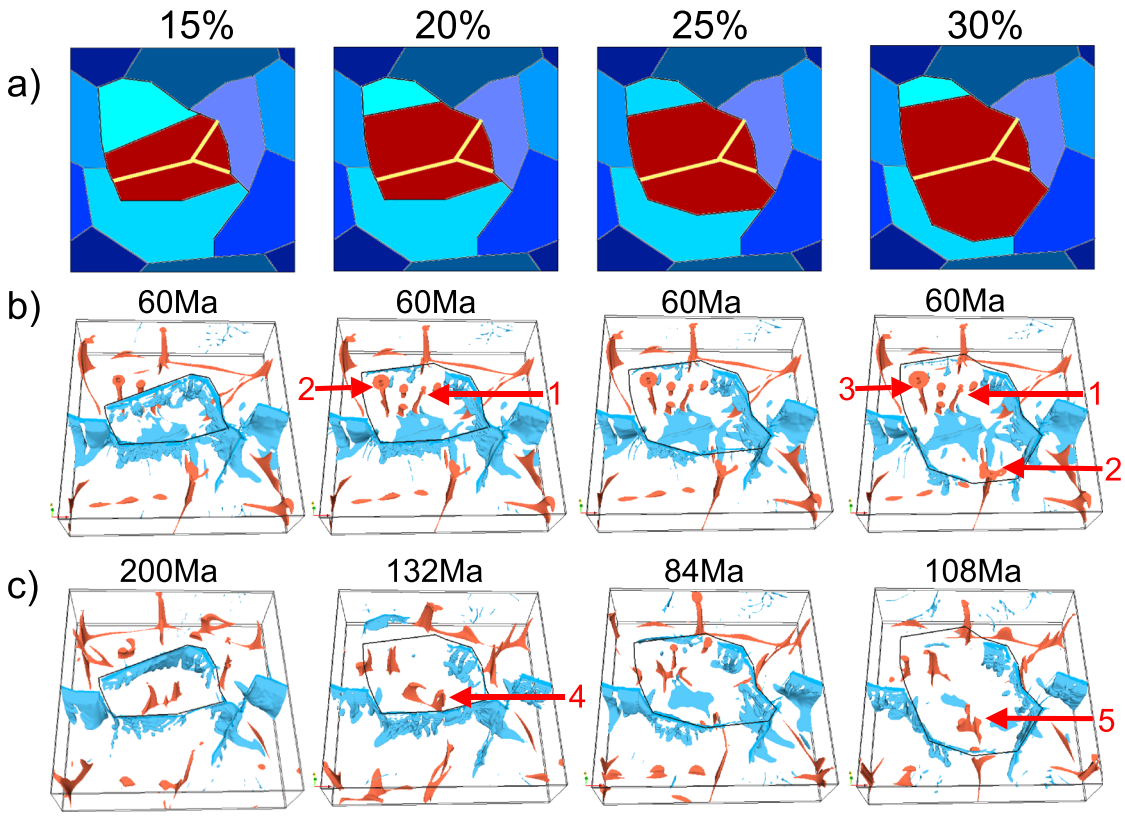

Figure 7. (a) 3-D plate geometry and (b–c) temperature snapshots showing plume formation at the specified time after supercontinent formation (using parameters given for Model D100_T5) when continent coverage is (left to right) 15% $(1.6d)^2$, 20% $(1.9d)^2$, 25% $(2.1d)^2$, and 30% $(2.3d)^2$ of the $4.25d \times 4.25d$ surface. The highlighted plumes correspond to the relevant panels in Figure 8.

$4.25 \times 4.25 \times 1$ solution domain is modeled. The grid resolution is $426 \times 426 \times 129$ for the high Rayleigh number models.

4.1. 3-D Initial Condition and Supercontinent Modeling

The initial condition for the supercontinent formation modeling in 3-D follows similar criteria to the 2-D study, insofar as plate motion convergence at a subduction zone brings continental material together above a thermally equilibrilated system. An initial condition is obtained by projecting a 2-D solution into the third dimension and then specifying a plate geometry featuring nine plates (Figure 6a). The Rayleigh number and parameters governing the viscous properties of the model are unchanged from the 2-D study (Table 1). The 3-D model is integrated forward in time (with the new plate geometry) until the system reaches a statistical steady state. As the model naturally evolves, an arrangement of convergent boundaries eventually develops, emulating the principal feature of the suture of the continental fragments that formed Pangea. Specifically, a Y-shaped plate boundary configuration [*Santosh et al.*, 2009] is obtained at the site of convergence of three large plates (A, B, and C, Figure 6a). In all 3-D models, the supercontinent is assembled through suturing three plates that converge at the Y-shaped arrangement of convergent boundaries above a similar Y-shaped downwelling configuration extending deep into the mantle (Figure 6b). Through changing the area of designated continental plates A, B, and C, the supercontinent size is varied to cover 15% $(1.6d)^2$, 20% $(1.9d)^2$, 25% $(2.1d)^2$, or 30% $(2.3d)^2$ of the surface (Figure 7a). The sizes of oceanic plates 4 and 7 are modified based on the area of the three plates joined to form the supercontinent (Figures 6a and 7a). The supercontinent is prescribed a velocity of zero relative to the net flow of the mantle and given an insulation parameter (i) of $^1/_4$ (when an insulating supercontinent is specified). The "initial" timeframe for plume generation is ~120 Myr, to allow time for a number of plumes to develop.

4.2. 3-D Models D100_T5

Figure 7 shows the downwelling and plume evolution in supercontinent formation models with varying continental coverage for case D100_T5, given the initial condition shown in Figure 6b. Due to the forces acting

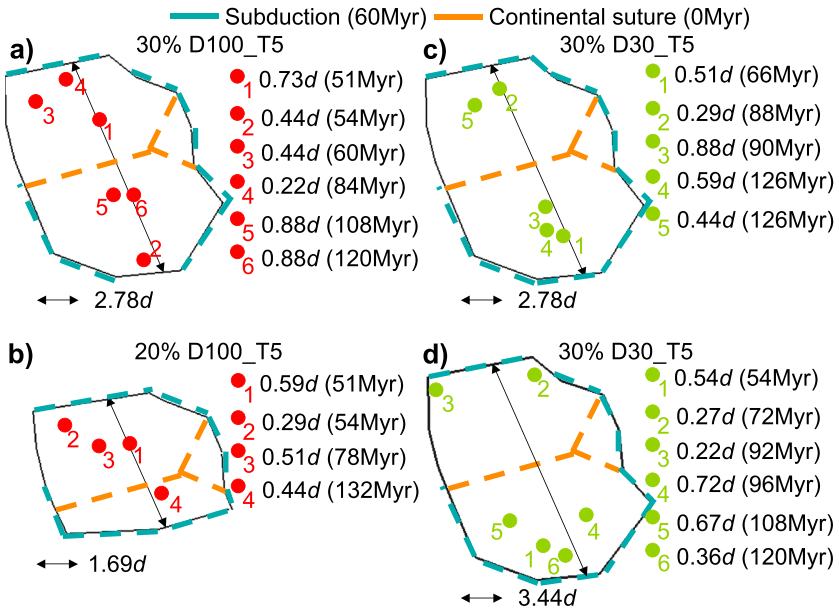

Figure 8. Subcontinent plume position as a function of time for 3-D study. Plumes that penetrate the 660 km boundary are recorded by position and time for: D100_T5 models (a) 30% $(2.3d)^2$ supercontinent with width across the center of the continent of $2.78d$ (as shown in Figures 7b and 7c) and (b) 20% $(1.9d)^2$ supercontinent with width across the center of $1.69d$ (as shown in Figures 7b and 7c), and D30_T5 models (c) 30% $(2.3d)^2$ supercontinent with width across the center of $2.78d$ (as shown in Figures 9e and 9f) and (d) 30% $(2.9d)^2$ supercontinent (using the larger $5.25d \times 5.25d$ surface) with width across the center of $3.44d$ (as shown in Figures 9h and 9i). The 0 Myr continental suture location (orange) and 60 Myr subduction location (teal) are also shown.

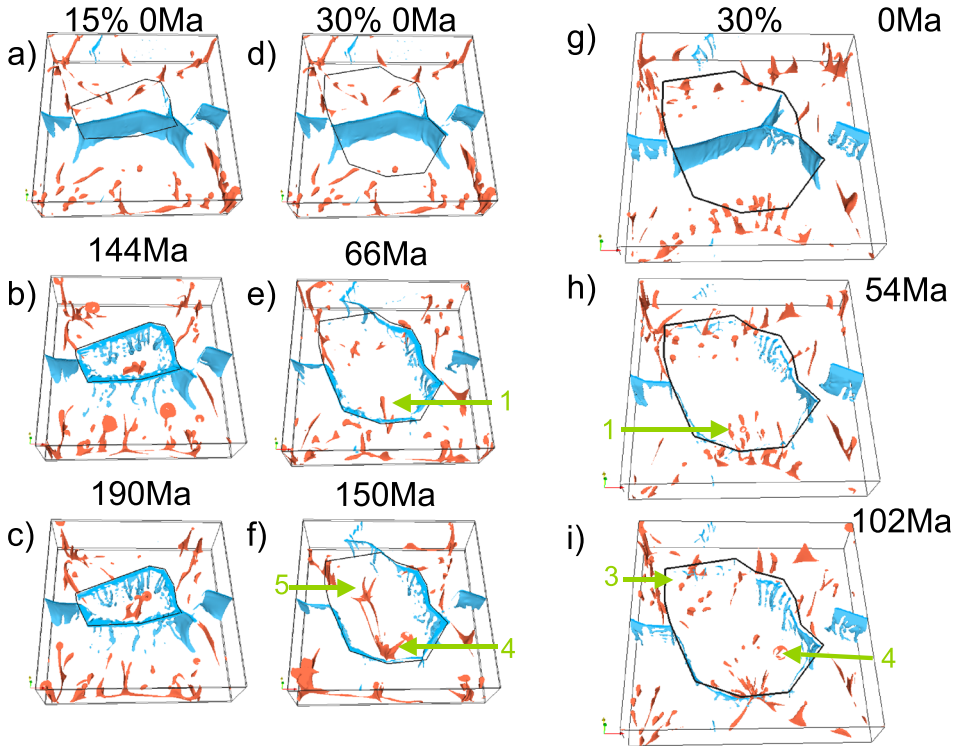

Figure 9. Temperature field snapshots for supercontinent models for the case D30_T5 when continental coverage is (a–c) 15% $(1.6d)^2$, (d–f) 30% $(2.3d)^2$ of a $4.25d \times 4.25d$ surface, and (g–i) 30% $(2.9d)^2$ of a $5.25d \times 5.25d$ surface (using the plate geometries shown in Figure 7a). The initial conditions for the models are given by snapshots (a), (d), and (g). The plume and subduction zone evolution is shown at the times specified in Figures 9b, 9c, 9e, 9f, 9h, and 9i post-supercontinent formation. The highlighted plumes correspond to the relevant panels in Figure 8.

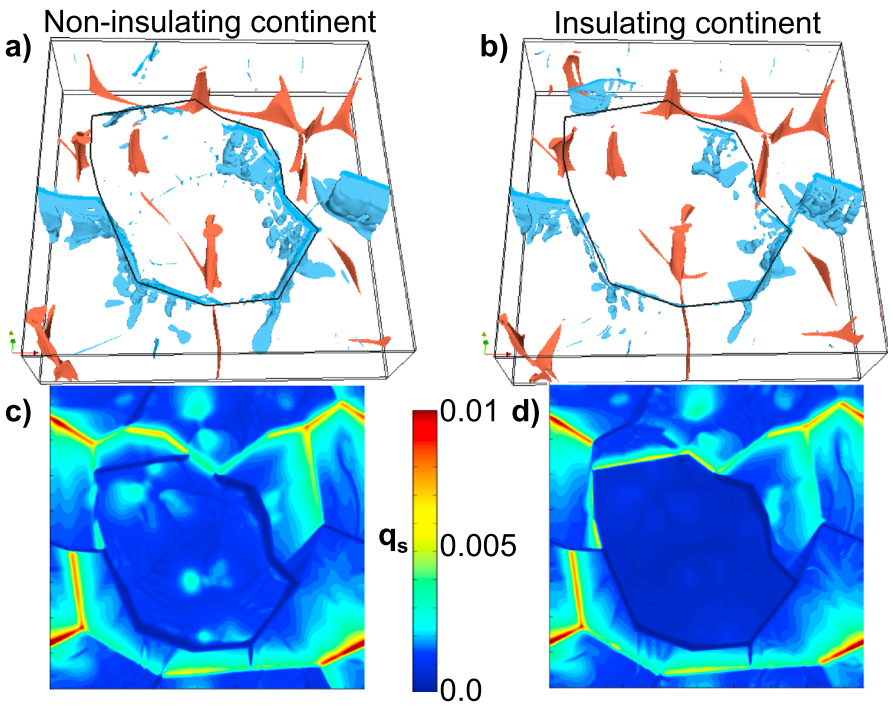

Figure 10. 3-D temperature and surface heat flux snapshots for models featuring a noninsulating and an insulating supercontinent covering 30% $(2.3d)^2$ of the surface using model D100_T5 parameters (in a $4.25d \times 4.25d \times d$ box). (a and c) Temperature and surface heat flux snapshots, respectively, 140 Myr after supercontinent formation for a noninsulating continent. (b and d) Temperature and surface heat flux snapshots, respectively, 140 Myr after supercontinent formation for an insulating continent.

on the plates following the cessation of subduction at the Y-shaped plate boundary, subduction moves to the edge of the supercontinent after its formation (e.g., Figure 7b). This evolution is similar to the scenario that gave rise to the formation of circum-Pangea subduction during the Permian (Figure 1). The primary plumes generated under a supercontinent covering more than 15% of the surface form close to the continental margins (Figure 7b). The residual mantle flow from the subduction at the continental suture interacts with mantle flow from the newly formed circum-supercontinent subduction to generate thermal instabilities near the core-mantle boundary (and produce mantle plumes). Figures 8a and 8b show the plume locations at the times when plumes first reach a depth of 660km for Model D100_T5 (covering 20%–30%). Plume arrival 1 (for both Figures 8a and 8b) and plume arrival 3 and 2 (Figures 8a and 8b, respectively) occur in the same region, despite having different circum-supercontinent subduction locations. This indicates that the remnant flow from the supercontinent formation subduction has a significant impact over continental margin subduction. For a supercontinent covering 15% of the surface, new plumes form under oceanic plates (Figure 7b) but primary plumes are absent below the supercontinent until much later (Figure 7c). For the largest continental coverage (25% and 30%), plumes arrive in ~20Myr intervals (e.g., three plumes occur around 60 Myr after formation, with further thermal anomalies at 80 Myr, 100 Myr, and 120 Myr (Figures 7c and 8a). As shown in Figure 8a, the first (primary) plume in the 30% $(2.3d)^2$ continental coverage case (which has a width across the middle of the continent of $2.78d$) forms at a distance $0.73d$ away from the continental margin (with secondary plumes, numbered 2 and 3, forming at a distance of $0.44d$ from the nearest continental margin). When compared to Figure 5a, this result is in-keeping with the findings of the 2-D study.

4.3. 3-D Models D30_T5

The four continental coverage scenarios of Figure 7a are also analyzed for the mantle parameters of Model D30_T5. Supercontinent formation is modeled in the same way as in D100_T5 (Figure 6) so that continental material aggregates over a downwelling. The smallest continental coverage case shown here features a subcontinental plume but only after an extensive period of time (Figures 9a–9c), as in the D100_T5 models. Increasing the continental coverage to 30% of the $4.25d \times 4.25d$ surface generates plumes close to the continental margins (Figures 9d–9f). Figure 8c shows the location of the plumes for the duration of the model's

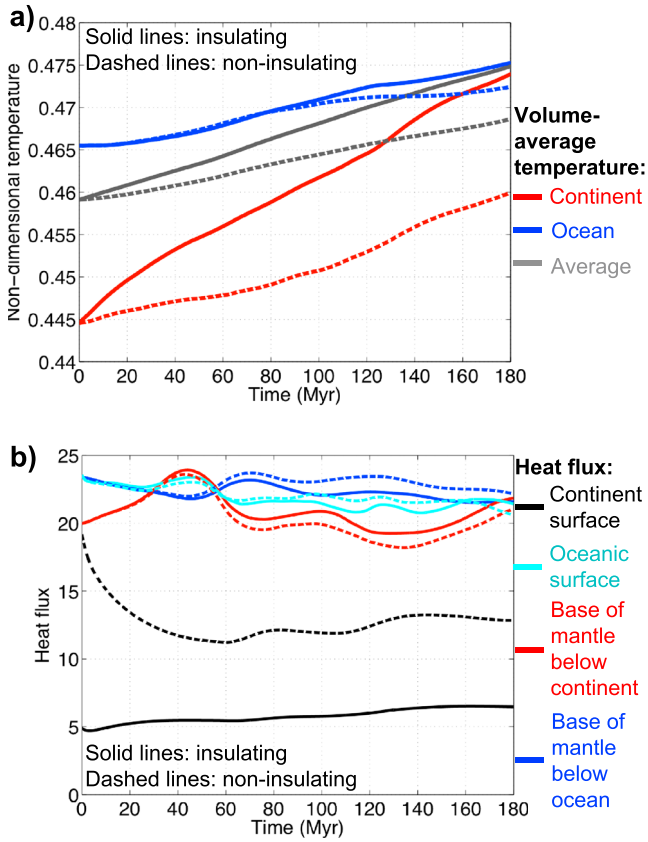

Figure 11. Time-series of (a) mean temperature below and (b) heat flux through an insulating (solid) and noninsulating (dashed) supercontinent (D100_T5) covering 30% of the $4.25d \times 4.25d \times d$ domain. The time-series in this figure correspond to the calculations that produced the snapshots shown in Figure 10.

evolution. The effect of reducing the lower mantle viscosity relative to that of the upper mantle locks the position of plume generation locations to the supercontinent subduction pattern (Figure 8c), as found in the 2-D study (Figure 5b). Figures 9g–9i show the response of the mantle to assembly of a larger continent (covering 30% of a $5.25d \times 5.25d$ surface). Despite the greater mantle volume existing under this continent, subcontinental plumes form in close proximity to the circum-supercontinent sites of subduction and not under the site of the continental suture downwelling location (Figure 8d).

4.4. Noninsulating Supercontinent

The effect of continental insulation on plume position is analyzed in Figure 10. Comparing temperature snapshots in supercontinent formation models featuring the mantle parameters of D100_T5 and a stationary continent covering 30% of the surface, Figures 10a and 10b show minor differences in mantle dynamics for models with and without enhanced continental insulation (a significant amount of time after the formation of the supercontinent). Through modeling oceanic and continental plates that cover the surface of the system, high heat flux is confined to the divergent plate boundaries (Figures 10c and 10d). Nevertheless, the effect of continental insulation on surface heat flux is highlighted when comparing a supercontinent with the thermal diffusivity of the oceanic material ($\kappa_c = \kappa$, Figure 10c) and one with a reduced oceanic thermal diffusivity ($\kappa_c = 0.25\kappa$, Figure 10d). Inhibiting continental surface heat flux mildly raises subsupercontinent temperatures and the volume-averaged temperature of the system (Figure 11a). The subcontinental build-up of heat does have an effect on circum-supercontinent and oceanic-oceanic subduction in the models, with downwellings being more prominent on the margins of the noninsulating supercontinent (Figure 10). However, the location of subcontinental and suboceanic mantle plumes are unaffected by continental insulation (Figure 9).

Figure 11 shows a 50% reduction in continental surface heat flux for the model featuring an insulating supercontinent. Surface heat flux from a noninsulating, stationary supercontinent is also significantly reduced when compared to an oceanic surface heat flux (Figure 11b). As a result, an increase in average mantle

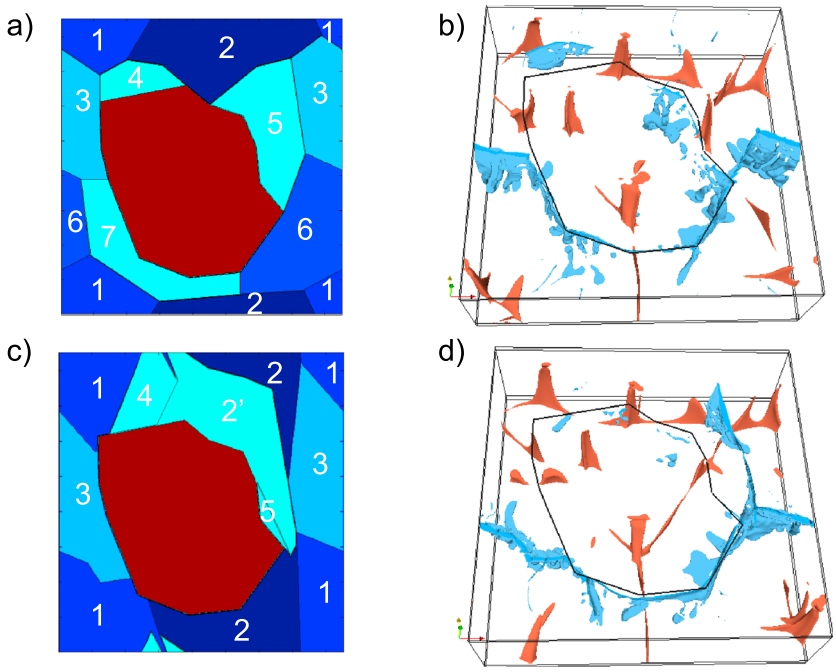

Figure 12. 3-D temperature snapshots comparing plume position for models featuring (a–b) nonevolving and (c–d) evolving oceanic plate boundaries 135 Myr after supercontinent formation (for Model D100_T5 with a supercontinent covering 30% of the $4.25d \times 4.25d$ surface). (a and c) Plate geometry and (b and d) temperature snapshots are compared for models started from the same initial condition (see Figure 6b).

temperature is observed for a simulation without enhanced continental insulation (dashed black line, Figure 11a). The increase in average mantle temperature is not as great as the simulation with enhanced continental insulation (solid black line, Figure 11a). Mantle basal heat flux below the continent shows a marginal increase in the continental insulation case, while mantle basal heat flux below the oceans is slightly decreased when compared to the noninsulating model (Figure 11b). The difference may be due to the repositioning of downwellings due to the build up of heat subcontinent. However, the differences in heat flux are small (aside from the surface heat flux from the insulating continent, which leads to an increase in mantle temperatures).

4.5. Changing Oceanic Subduction Location

In this section a supercontinent formation model with evolving oceanic boundaries is compared to a model with fixed plate boundaries, where both models feature the mantle parameters of case D100_T5. The modeling of plate evolution with mobile oceanic boundaries is highly idealized but permits the analysis of first-order processes relating to the thermal evolution of mantle temperatures post-supercontinent formation (e.g., how changing oceanic-oceanic subduction location affects subcontinental mantle dynamics). The oceanic-oceanic plate triple junctions move with a velocity equal to the area weighted mean of the adjacent plates [e.g., *Gait et al.*, 2008; *Stein and Lowman*, 2010]. However, the continental boundaries are stationary (as before, the supercontinent has no velocity relative to the net flow of the mantle). Oceanic plate boundaries that meet the supercontinent perimeter migrate along the margin of the continent (so that the continental size and shape remains the same for the duration of the calculation (Figure 12)). An arbitrary "plate age" is assigned and then used to determine which oceanic plate would be subducted at an oceanic-oceanic boundary. A "younger" oceanic plate (determined by the numbering system in Figure 12a, with 1 (youngest) and 7 (oldest)) maintains its shape as the "older" oceanic plate is modified (simulating subduction of the older oceanic material under a younger plate). As the model evolves, oceanic plates are fractured if they become large enough that internal stresses would instigate breakup (here it is specified that when an oceanic plate covers over 25% of the model surface the plate should break along an arbitrarily chosen line of fracture).

Allowing the oceanic plate geometry to evolve has a dramatic effect on the shape and number of the oceanic plates, even after a fraction of a mantle transit time (compare Figures 12a and 12c). Figures 12b and 12d show the difference in subduction zone location between the two calculations 135 Myr after supercontinent

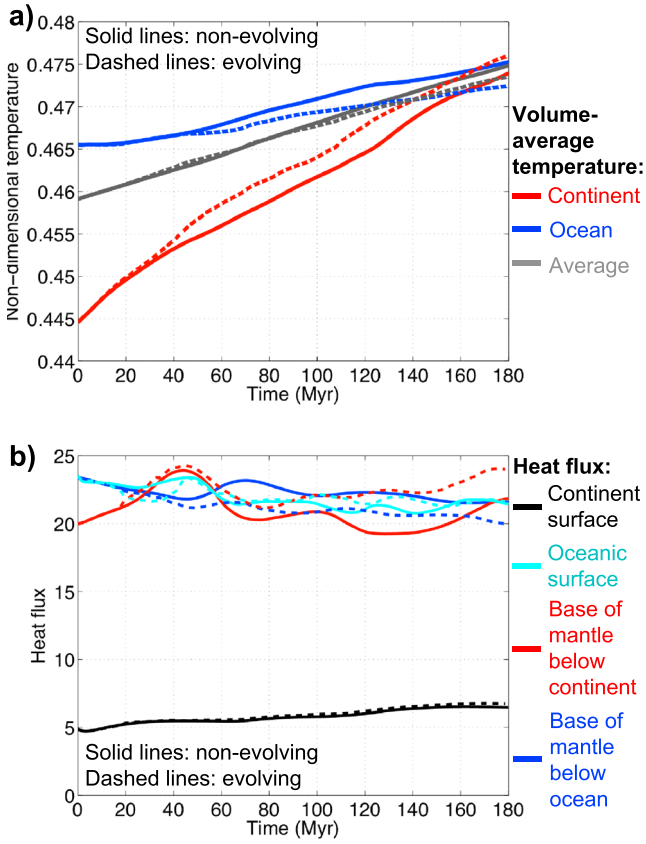

Figure 13. Time series of (a) mean temperature below and (b) heat flux through an insulating supercontinent with nonevolving oceanic plates (solid) and a model with evolving oceanic plates (dashed). The time-series in this figure correspond to the calculations that produced the snapshots shown in Figure 12.

formation. Although there are some differences in subduction locations on the supercontinent margins, the stationarity of the supercontinent forms similar subduction patterns resulting in the formation of subcontinental plumes in roughly the same location for both calculations. Furthermore, suboceanic plume locations remain similar on the timescale associated with supercontinent assembly, despite the evolution of the oceanic boundaries.

In the calculation with evolving oceanic boundaries on supercontinent timescales, subcontinental temperatures below the insulating supercontinent are marginally higher than subcontinental temperatures with fixed oceanic boundaries (Figure 13a). The free evolution of the oceanic boundaries generates greater subducted material on the supercontinent margin to draw in more subcontinental heat from the core (red lines, Figure 13b), which can account for the increase in subcontinental temperature. When oceanic plate size and shape are allowed to evolve (dashed blue line, Figure 13a), a smaller increase in suboceanic temperature can also be accounted for by a relative decrease in suboceanic basal heat flux (blue lines, Figure 13b) as compared to when oceanic plate boundaries are fixed. However, more calculations (using larger solution domains) are required in order to further understand the effect of mobile oceanic plate boundaries on mantle temperatures.

5. Discussion

Results from our 2-D and 3-D modeling show that changing the viscosity structure for mantle convection simulations (with similar surface heat flux) can determine the position (and number) of subcontinental plumes penetrating the upper mantle post-supercontinent formation (e.g., Figures 5, 7, and 9). Furthermore, post-supercontinent formation, the subcontinental plume locations observed with the four mantle viscosity models considered (Figure 2c) show varying degrees of dependence on the location of continent margin subduction (Figure 5).

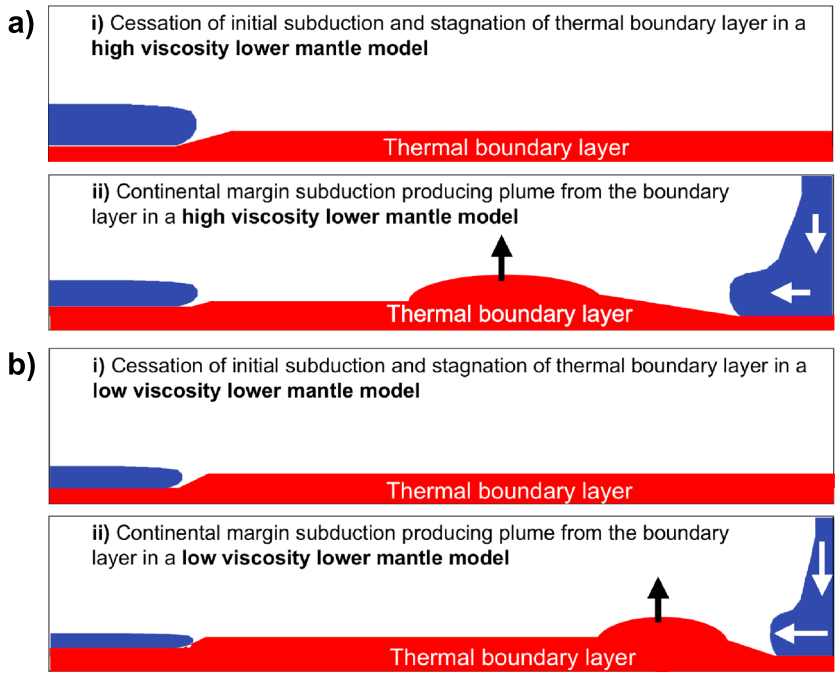

Figure 14. Thermal boundary layer analysis for (a) high and (b) low lower mantle viscosities (relative to the reference viscosity featured in the Rayleigh number Ra_0). A high lower mantle viscosity broadens the features of mantle dynamics. Broad downwellings arriving at the core-mantle boundary both pinch and thicken the thermal boundary layer in the immediate vicinity and further away from the slab, respectively (Figure 14a, ii). The generation of thermal instabilities produces plumes from the thermal boundary layer. The same process occurs for a low lower mantle viscosity; however, the boundary layer instability is not as broad. Therefore, the thickening occurs at a shorter distance from the new slab. The high viscosity lower mantle has slower mantle velocities than the lower viscosity lower mantle, as indicated by the arrows on the downwelling slabs.

For 2-D models featuring a high contrast in the geotherm-dependent viscosity ($\Delta\eta = 10^7$) with continental coverage $\geq 1.6d$ (e.g., $>$ 15% coverage), plume positions occur well away from the location below the continental suture (Figures 5c and 5d). For supercontinental coverage $\geq 2.8d$, in a system featuring two subcontinental plumes, primary and secondary plume locations appear to be locked to positions between $0.8d$ (2320 km) and $1.0d$ (2900 km) from the continental margin subduction. Consequently, subcontinental plume position shows no dependence on the location of continental suture subduction (Figures 5c and 5d). 2-D and 3-D D30_T5 models show similar results for the same continental coverage, with primary plume formation occurring at a distance between $0.6d$ (1740 km) and $0.8d$ (2320 km) from the site of continent margin subduction in the 2-D study (Figure 5b).

The viscosity profile featuring the relatively weakest geotherm-dependence (D100_T5, Figure 2c) allows for the greatest departure of the subcontinental primary plumes from a position locked to continental margin subduction (Figure 5a). Cold downwellings in the lower mantle are broad in Model D100_T5 due to the relatively high viscosity in the lower mantle (Figure 2c). After the cessation of subduction at the continental suture, the subcontinental bottom thermal boundary layer becomes stagnant (Figure 14a). The arrival of the broad downwelling formed at the edge of the supercontinent pinches the thermal boundary layer and increases heat flow into the base of the mantle. The cold slab produces a thickening of the thermal boundary layer away from the downwelling region (toward the center of the subcontinental region, Figure 14b) that becomes unstable (generating a plume). For models with a smaller viscosity contrast between the upper and lower mantle, subducted material does not form such broad features. The impact of material from the continental margin downwelling on the stagnant lower thermal boundary layer still produces thermal instabilities (and eventual plumes) due to the generation of enhanced horizontal temperature gradients in the squeezed boundary layer. However, the thickening of the thermal boundary layer occurs closer to the new subduction location as a result of the smaller wavelength features associated with the lower viscosity (Figures 14c and 14d). Nevertheless, for all viscosity profiles that feature more than one subcontinental plume and a

Table 2. Approximation of LIP Position Relative to Continental Margin Subduction Location[a]

LIP	Symbol	Age	Lat	Long	LIP Distance From Subduction
CAMP	CP	200 Ma	2.5	341.9	~2400 km (0.8*d*)
Karoo Ridge	KR	182 Ma	−44.6	2.8	~3300 km (1.1*d*)
Bunbury Basalts	BU	132 Ma	−55.3	81.6	~3100 km (1.1*d*)

[a]The three LIPs analyzed are inferred to have formed from primary plumes in a subcontinental region post-supercontinent formation (and after 250 Ma). Latitude (Lat) and longitude (Long) values are taken from *Torsvik et al.* [2008] and give the location of reconstructed plume centers. LIP distance from nearest subduction location is an approximation. As a first-order approximation, the LIP center is measured to the nearest continental margin at 300 Ma to give the LIP distance from subduction (prior to any dispersal).

large supercontinent (e.g., coverage greater than 2.8*d*), calculations show no clear correlation between plume location and the location of continental suture at the precollision subduction site.

Comparing models with and without evolving oceanic boundaries shows few changes in the subcontinental dynamics on timescales relevant to the generation of subcontinental plumes (Figure 12). Thus, isolation from subduction under the supercontinent creates an isolated environment unique to the supercontinent cycle [e.g., *Phillips and Coltice*, 2010; *Lenardic et al.*, 2011]. Furthermore, in cases featuring plate boundary evolution, suboceanic plume positions show little lateral movement during the period relevant to supercontinent assembly, despite the repositioning of subduction zones in the evolving boundary models (Figure 12). This result is consistent with those of *Lowman et al.* [2008] who found a viscosity contrast between the upper and lower mantle of a factor of 100 anchors plume locations for well in excess of a surface transit time (e.g., the time taken to travel the mantle depth using the mean surface velocity).

In the analysis of numerical models featuring both kinematic plate velocities and thermochemical piles, it is difficult to determine which is more influential: compositionally anomalous provinces in the generation of plumes or subduction in the lateral movement of the compositional piles. However, the study presented here establishes a link between subduction location and the generation of plumes in models that do not feature thermochemical piles but do feature dynamic plate velocities. If compositionally anomalous provinces are believed to only play a secondary role in mantle dynamics [*Davies et al.*, 2012], then the past (and future) locations of large igneous provinces can be, in part, explained by subduction zone location and the contrast between upper and lower mantle viscosity. Using Monte-Carlo based statistics, *Austermann et al.* [2014] recently conducted a statistical analysis of the correlation between large igneous provinces and lower mantle seismic structure to test whether plumes are preferentially generated at the margins of LLSVPs. Their results show that large igneous provinces correlate with both the margins and the interior of LLSVPs, with the two correlations being indistinguishable. Accordingly, *Austermann et al.* [2014] argue the identification of "plume generation zones" with the LLSVP margins [e.g., *Torsvik et al.*, 2006; *Burke et al.*, 2008; *Torsvik et al.*, 2008, 2010] to be premature.

If thermochemical piles on the core-mantle boundary do not play a role in the formation of subcontinental plumes then subduction on its own may be a driving force for gathering lower mantle thermal instabilities. However, it is difficult to identify which paleosubduction zone interacted with the mantle's lower thermal boundary later to produce a given LIP (e.g., Figure 1) due to uncertainties that include plume rise time and slab sinking rate. This is particularly the case with LIPs such as Skagerrak (SK, 297 Ma, Figure 1) and the Siberian Traps (ST, 251 Ma, Figure 1), which formed too early after 300 Ma to be influenced by the circum-supercontinent subduction shown in Figure 1.

The role of continental dispersal (and therefore the evolution of continental margin subduction) in the generation of mantle plumes is not featured in this study. However, a dispersing supercontinent would have an impact on mantle dynamics (particularly for secondary plumes forming after continental dispersal has begun). As a result, only subcontinental plumes that form a short time after supercontinent formation are analyzed (i.e., "initial" plumes forming in the first 90 Myr post-supercontinent formation). Therefore, only primary LIPs for a given subcontinental region (e.g., Central Atlantic Magmatic Province (CP, 200 Ma), Karoo Ridge (KR, 182 Ma), and Bunbury Basalts (BU, 132 Ma), Figure 1) can be compared to the plumes from our numerical models. For these three LIPs, Table 2 gives the approximate values of the nearest continental

margin paleosubduction zone (before continental dispersal occurs at 300 Ma) relative to the primary plume center location (with the subduction locations and plume positions taken from Figure 1). The three LIPs form within ~0.8*d* (~2300 km) and ~1.1*d* (~3200 km) of the nearest 300 Ma continental margin (as highlighted in Figure 1). Comparing these observations with the results in Figure 5 shows Models D100_T7 and D30_T7 feature viscosity profiles consistent with post-Pangean dynamics (e.g., plumes form at a distance between 0.7*d* and 1.0*d* for a supercontinent with a large width). However, a limitation of our study is the use of the Cartesian geometry to model a spherical geometry setting. The geometry of the solution domain is likely to influence details in the position of the plumes. In a spherical geometry plumes diverge as they rise from the core-mantle boundary (e.g., a separation of *d* at the CMB becomes 1.8*d* at the surface) and sinking slabs converge. Therefore, refining expected separations of subduction zones and plume derived LIPs in an isochemical mantle requires the use of spherical geometry models. Furthermore, although geotherm-dependent viscosity has been shown to approximate fully temperature dependent viscosity for obtaining first-order dynamics [*Stein and Hansen*, 2014], slabs with lateral variation in viscosity would also be preferable in future studies. Other influences on the position of plumes relative to continental margins may include a net rotation of the surface, a background mantle flow, and an endothermic phase boundary at 660km (or elsewhere).

Future modeling work would greatly benefit from additional subduction history information prior to 300 Ma. If chemical piles are greatly influenced by downwellings reaching the core-mantle boundary [e.g., *Tackley*, 1998; *Kellogg et al.*, 1999; *Jellinek and Manga*, 2002; *McNamara and Zhong*, 2005; *Zhang et al.*, 2010; *Tan et al.*, 2011; *Li and McNamara*, 2013] and are only passive in the development of plumes [e.g., *Davies et al.*, 2012], then subduction locations must strongly influence the position of large igneous provinces. The results here use the available geophysical and geological data to choose an initial condition featuring a possible scenario consistent with supercontinent formation conditions. Nevertheless, better knowledge of subduction locations during the formation of Pangea would help to recreate subsupercontinent thermal conditions. A cross-field study using geological fieldwork and geodynamic modelling may help constrain subduction locations from earlier than 300 Ma (as the the age of the surface features that pertain to pre-Pangean subduction and the unconstrained corresponding paleolongitude currently make it difficult to analyze). Geological field samples combined with smaller-scale lithospheric geodynamic models may help to further constrain a pre-Pangea initial condition. Similarly, the evolution of the Rheic ocean has been highlighted as important in the final stages of the formation of Pangea [*Nance et al.*, 2010, 2012]. As a result, future work should be conducted on geodynamic modeling of the Rheic ocean evolution to generate a better understanding of the thermal state of the subsupercontinent mantle.

6. Conclusion

This study analyzes the role of subduction and mantle viscosity in the generation of subcontinental mantle plumes in supercontinent formation models. We find that once a critical supercontinent width is reached, plumes do not form under the center of a supercontinent (i.e., the site of previous subduction). In 2-D studies featuring a lower viscosity lower mantle or an inherent depth-dependent viscosity contrast mitigated by a strong thermal viscosity contrast (e.g., Models D30_T5, D30_T7, and D100_T7), the plume positions beneath the continent become locked to the continental margins (Figures 5b–5d) at a distance of 0.6*d* to 1.0*d* (~2000–3000 km). The broad downwellings in simulations that feature increased lower mantle viscosity (e.g., D100_T5) generate longer wavelength perturbations in the basal thermal boundary layer (Figure 14), leading to plumes forming at a greater distance from the continent margin subduction site than is observed in calculations featuring the other viscosity profiles modeled (Figure 5). However, for all mantle viscosity profiles, in both 2-D and 3-D studies, subcontinental plume positions show dependence on the location of supercontinent margin subduction (again, once a critical continent size has been reached).

The study concludes that the role of subduction is important in the generation and location of subcontinental mantle plumes. As theories differ on the role of chemical piles in plume formation [e.g., *Tackley*, 1998; *Kellogg et al.*, 1999; *Jellinek and Manga*, 2002; *McNamara and Zhong*, 2005; *Torsvik et al.*, 2006; *Burke et al.*, 2008; *Torsvik et al.*, 2008; *O'Neill et al.*, 2009; *Torsvik et al.*, 2010; *Zhang et al.*, 2010; *Tan et al.*, 2011; *Li and McNamara*, 2013], it is significant that our isochemical models show mantle viscosity and subduction to be controlling

factors in plume generation post-supercontinent formation. If LLSVPs are the result of purely thermal structures, or a passive thermochemical anomaly, the results of the 2-D and 3-D studies show that the formation of subduction zones at the margins of a supercontinent (and indeed supercontinent forming subduction) has a profound effect on mantle dynamics and may help to explain how the sites of large igneous provinces were (and will be) determined.

Acknowledgments

We thank Bernhard Steinberger for providing the paleosubduction data in Figure 1 and Adrian Lenardic for his support and encouragement of this study. We also thank two anonymous referees and the Associate Editor (Mark D. Behn) for constructive reviews. J. P. L. is grateful for funding from the NSERC of Canada (fund 327084-10). C. S. is grateful for funding from the DFG (grant HA1765/24-1). Computations were performed on the GPC supercomputer at the SciNet HPC Consortium [*Loken et al.*, 2010]. SciNet is funded by the Canada Foundation for Innovation under the auspices of Compute Canada, the Government of Ontario, Ontario Research Fund–Research Excellence, and the University of Toronto. Data from this study can be made available from P. J. H.

References

Austermann, J., B. T. Kaye, J. X. Mitrovica, and P. Huybers (2014), A statistical analysis of the correlation between large igneous provinces and lower mantle seismic structure, *Geophys. J. Int.*, *197*, 1–9, doi:10.1093/gji/ggt500.

Brandenburg, J. P., and P. E. van Keken (2007), Methods for thermochemical convection in Earth's mantle with force-balanced plates, *Geochem. Geophys. Geosyst.*, *8*, Q11004, doi:10.1029/2007GC001692.

Bull, A. L., A. K. McNamara, and J. Ritsema (2009), Synthetic tomography of plume clusters and thermochemical piles, *Earth Planet. Sci. Lett.*, *278*, 152–162.

Burke, K., and T. H. Torsvik (2004), Derivation of large igneous provinces of the past 200 million years from long-term heterogeneities in the deep mantle, *Earth Planet. Sci. Lett.*, *227*, 531–538.

Burke, K., B. Steinberger, T. H. Torsvik, and M. A. Smethurst (2008), Plume generation zones at the margins of large low shear velocity provinces on the core-mantle boundary, *Earth Planet. Sci. Lett.*, *265*, 49–60.

Chandrasekhar, S. (1961), *Hydrodynamic and Hydromagnetic Stability*, Oxford Univ. Press, New York.

Courtillot, V., C. Jaupart, I. Manighetti, P. Taponier, and J. Besse (1999), On causal links between flood basalts and continental breakup, *Earth Planet. Sci. Lett.*, *166*, 177–195.

Davies, R. D., S. Goes, J. H. Davies, B. S. A. Schuberth, H.-P. Bunge, and J. Ritsema (2012), Reconciling dynamic and seismic models of Earth's lower mantle: The dominant role of thermal heterogeneity, *Earth Planet. Sci. Lett.*, *353–354*, 253–269.

Ernst, R. E., and W. Bleeker (2010), Large igneous provinces (LIPs), giant dyke swarms, and mantle plumes: Significance for breakup events within Canada and adjacent regions from 2.5 Ga to the Present, *Can. J. Earth Sci.*, *47*(5), 695–739.

Ernst, R. E., K. L. Buchan, and I. H. Campbell (2005), Frontiers in large igneous province research, *Lithos*, *79*, 271–297.

Foley, B., and T. W. Becker (2009), Generation of plate tectonics and mantle heterogeneity from a spherical, visco-plastic convection model, *Geochem. Geophys. Geosyst.*, *10*, Q08001, doi:10.1029/2009GC002378.

Gable, C. W., R. J. O'Connell, and B. J. Travis (1991), Convection in three dimensions with surface plates: Generation of toroidal flow, *J. Geophys. Res.*, *96*, 8391–8405.

Gait, A. D., J. P. Lowman, and C. W. Gable (2008), Time dependence in 3-D mantle convection models featuring evolving plates: Effect of lower mantle viscosity, *J. Geophys. Res.*, *113*, B08409, doi:10.1029/2007JB005538.

Gurnis, M. (1988), Large-scale mantle convection and the aggregation and dispersal of supercontinents, *Nature*, *332*, 695–699.

Heron, P. J. (2014), Mantle dynamics following supercontinent formation, PhD thesis, p. 173, Univ. of Toronto, Canada.

Heron, P. J., and J. P. Lowman (2010), Thermal response of the mantle following the formation of a "super-plate", *Geophys. Res. Lett.*, *37*, L22302, doi:10.1029/2010GL045136.

Heron, P. J., and J. P. Lowman (2011), The effects of supercontinent size and thermal insulation on the formation of mantle plumes, *Tectonophysics*, *510*, 28–38.

Heron, P. J., and J. P. Lowman (2014), The impact of Rayleigh number on assessing the significance of supercontinent insulation, *J. Geophys. Res. Solid Earth*, *119*, 711–733, doi:10.1002/2013JB010484.

Hofmeister, A. M. (1999), Mantle values of thermal conductivity and the geotherm from phonon lifetimes, *Science*, *283*(5408), 1699–1706, doi:10.1126/science.283.5408.1699..

Honda, S., M. Yoshida, S. Ootorii, and Y. Iwase (2000), The timescales of plume generation caused by continental aggregation, *Earth Planet. Sci. Lett.*, *176*, 31–43.

Jellinek, A. M., and M. Manga (2002), The influence of a chemical boundary layer on the fixity and lifetime of mantle plumes, *Nature*, *418*, 760–763, doi:10.1038/nature00979.

Kellogg, L. H., B. H. Hager, and R. van der Hilst (1999), Compositional stratification in the deep mantle, *Science*, *283*, 1881–1884, doi:10.1126/science.283.5409.1881.

King, S. D., C. W. Gable, and S. A. Weinstein (1992), Models of convection-driven tectonic plates: A comparison of methods and results, *Geophys. J. Int.*, *109*, 481–487.

Koglin, D. E. Jr., S. R. Ghias, S. D. King, G. T. Jarvis, and J. P. Lowman (2005), Mantle convection with reversing mobile plates: A benchmark study, *Geochem. Geophys. Geosyst.*, *6*, Q09O03, doi:10.1029/2005GC000924.

Korenaga, J. (2010), Scaling of plate-tectonic convection with pseudoplastic rheology, *J. Geophys. Res.*, *115*, B11405, doi:10.1029/2010JB007670.

Lenardic, A., L.-N. Moresi, A. M. Jellinek, and M. Manga (2005), Continental insulation, mantle cooling, and the surface area of oceans and continents, *Earth Planet. Sci. Lett.*, *234*, 317–333.

Lenardic, A., L.-N. Moresi, A. M. Jellinek, C. O'Neill, C. M. Cooper, and C. T. Lee (2011), Continents, supercontinents, mantle thermal mixing, and mantle thermal isolation: Theory, numerical simulations, and laboratory experiments, *Geochem. Geophys. Geosyst.*, *12*, Q10016, doi:10.1029/2011GC003663.

Li, M., and A. K. McNamara (2013), The difficulty for subducted oceanic crust to accumulate at the Earth's core-mantle boundary, *J. Geophys. Res. Solid Earth*, *118*, 1807–1816, doi:10.1002/jgrb.50156.

Loken, C., et al. (2010), SciNet: Lessons learned from building a power-efficient top-20 system and data centre, *J. Phys. Conf. Ser.*, *256*, 012026, doi:10.1088/1742-6596/256/1/012026.

Lowman, J. P., and G. T. Jarvis (1995), Mantle convection models of continental collisions and breakup incorporating finite thickness plates, *Phys. Earth Planet. Inter.*, *88*, 53–68.

Lowman, J. P., A. D. Gait, C. W. Gable, and H. Kukreja (2008), Plumes anchored by a high viscosity lower mantle in a 3D mantle convection model featuring dynamically evolving plates, *Geophys. Res. Lett.*, *35*, L19309, doi:10.1029/2008GL035342.

McNamara, A. K., and S. J. Zhong (2005), Thermochemical structures beneath Africa and the Pacific Ocean, *Nature*, *437*, 1136–1139, doi:10.1038/nature04066.

Moresi, L., and V. Solomatov (1995), Numerical investigation of 2D convection with extremely large viscosity variations, *Phys. Fluids*, *7*, 2154–2162.

Nance, R. D., G. Gutiérrez-Alonso, J. D. Keppie, U. Linnemann, J. B. Murphy, C. Quesada, R. A. Strachan, and N. H. Woodcock (2010), Evolution of the Rheic Ocean, *Gondwana Res.*, *17*, 194–222.

Nance, R. D., G. Gutiérrez-Alonso, J. D. Keppie, U. Linnemann, J. B. Murphy, C. Quesada, R. A. Strachan, and N. H. Woodcock (2012), A brief history of the Rheic Ocean, *Geosci. Front.*, *3*, 125–135.

O'Farrell, K., and J. P. Lowman (2010), Emulating the thermal structure of spherical shell convection in plane-layer geometry mantle convection models, *Phys. Earth Planet. Inter.*, *182*, 73–84.

O'Neill, C., and A. Lenardic (2007), Geological consequences of super-sized Earths, *Geophys. Res. Lett*, *34*, L19204, doi:10.1029/2007GL030598.

O'Neill, C., A. Lenardic, A. M. Jellinek, and L. Moresi (2009), Influence of supercontinents on deep mantle flow, *Gondwana Res.*, *15*, 276–287.

Phillips, B. R., and N. Coltice (2010), Temperature beneath continents as a function of continental cover and convective wavelength, *J. Geoph. Res.*, *115*, B04408, doi:10.1029/2009JB006600.

Rolf, T., N. Coltice, and P. J. Tackley (2012), Linking continental drift, plate tectonics and the thermal state of the Earth's mantle, *Earth Planet. Sci. Lett.*, *351–352*, 134–146.

Santosh, M., S. Maruyama, and S. Yamamoto (2009), The making and breaking of supercontinents: Some speculations based on superplumes, super downwelling and the role of tectosphere, *Gondwana Res.*, *15*(3–4), 324–341.

Schubert, G., D. L. Turcotte, and P. Olson (2001), *Mantle Convection in the Earth and Planets*, 940 pp., Cambridge Univ. Press, New York.

Schubert, G., G. Masters, P. Olson, and P. Tackley (2004), Superplumes or plume clusters?, *Phys. Earth Planet. Inter.*, *146*, 147–162.

Scotese, C. R. (2001), Atlas of Earth history, *PALEOMAP Progress Rep. 90/0497*, Dep. of Geol., Univ. of Tex. at Arlington, Arlington.

Stein, C., and J. P. Lowman (2010), Response of mantle heat flux to plate evolution, *Geophys. Res. Lett.*, *37*, L24201, doi:10.1029/2010GL045283.

Stein, C., J. Schmalzl, and U. Hansen (2004), The effect of rheological parameters on plate behaviour in a self-consistent model of mantle convection, *Phys. Earth Planet. Inter.*, *142*, 225–255.

Stein, C., J. P. Lowman, and U. Hansen (2013), The influence of mantle internal heating on lithospheric mobility: Implications for super-Earths, *Earth Planet Sci. Lett.*, *361*, 448–459.

Stein, C., J. P. Lowman, and U. Hansen (2014), A comparison of mantle convection models featuring plates, *Geochem. Geophys. Geosyst.*, *15*, 2689–2698, doi:10.1002/2013GC005211.

Stein, C., and U. Hansen (2014), Numerical investigation of a layered temperature-dependent viscosity convection in comparison to convection with a full temperature dependence, *Phys. Earth Planet. Inter.*, *226*, 1–13.

Steinberger, B., and T. H. Torsvik (2012), A geodynamic model of plumes from the margins of Large Low Shear Velocity Provinces, *Geochem. Geophys. Geosyst.*, *13*, Q01W09, doi:10.1029/2011GC003808.

Tackley, P. J. (1998), Three-dimensional simulations of mantle convection with a thermochemical CMB boundary layer: D"?, in *The Core-Mantle Boundary Region, Geodyn. Ser.*, vol. 28, edited by M. Gurnis, pp. 231–253, AGU, Washington, D. C.

Tackley, P. J. (2000), Self-consistent generation of tectonic plates in time-dependent, three-dimensional mantle convection simulations. Part 1: Pseudoplastic yielding, *Geochem. Geophys. Geosyst.*, *1*, 1021, doi:10.1029/2000GC000036.

Tan, E., W. Leng, S. Zhong, and M. Gurnis (2011), On the location of plumes and lateral movement of thermochemical structures with high bulk modulus in the 3-D compressible mantle, *Geochem. Geophys. Geosyst.*, *12*, Q07005, doi:10.1029/2011GC003665.

Torsvik, T. H., M. A. Smethurst, K. Burke, and B. Steinberger (2006), Large igneous provinces generated from the margins of the large low-velocity provinces in the deep mantle, *Geophys. J. Int*, *167*, 1447–1460.

Torsvik, T. H., B. Steinberger, R. M. Cocks, and K. Burke (2008), Longitude: Linking Earth's ancient surface to its deep interior, *Earth Planet. Sci. Lett.*, *276*, 273–282.

Torsvik, T. H., K. Burke, B. Steinberger, S. J. Webb, and L . D. Ashwal (2010), Diamonds sampled by plumes from the core-mantle boundary, *Nature*, *466*, 352–355, doi:10.1038/nature09216.

Trubitsyn, V. P., and V. V. Rykov (1995), A 3-D numerical model of the Wilson cycle, *J. Geodyn.*, *20*(1), 63–75.

van Heck, H. J., and P. J. Tackley (2008), Planforms of self-consistently generated plates in 3-D spherical geometry, *Geophys. Res. Lett*, *35*, L19312, doi:10.1029/2008GL035190.

Yale, L. B., and S. J. Carpenter (1998), Large igneous provinces and giant dike swarms: Proxies for supercontinent cyclicity and mantle convection, *Earth Planet. Sci. Lett.*, *163*, 109–122.

Yoshida, M., and M. Santosh (2011), Supercontinents, mantle dynamics and plate tectonics: A perspective based on conceptual vs. numerical models, *Earth Sci. Rev.*, *105*, 1–24.

Yoshida, M., Y. Iwase, and S. Honda (1999), Generation of plumes under a localized high viscosity lid in 3-D spherical shell convection, *Geophys. Res. Lett.*, *26*(7), 947–950.

Zhang, N., S. J. Zhong, W Leng, and Z. X. Li (2010), A model for the evolution of the Earth's mantle structure since the Early Paleozoic, *J. Geophys. Res.*, *115*, B06401, doi:10.1029/2009JB006896.

Zhong, S., and M. Gurnis (1993), Dynamic feedback between a continent like raft and thermal convection, *J. Geophys. Res.*, *98* (7), 12,219–12,232.

Zhong, S., M. T. Zuber, L. Moresi, and M. Gurnis (2000), Role of temperature dependent viscosity and surface plates in spherical shell models of mantle convection, *J. Geophys. Res.*, *105*, 11,063–11,082.

Zhong, S. J., N. Zhang, Z. X. Li, and J. Roberts (2007), Supercontinent cycles, true polar wander, and very long wavelength mantle convection, *Earth Planet. Sci. Lett.*, *375*, 115–122.